IEEE Access
Multidisciplinary | Rapid Review | Open Access Journal

Received June 24, 2019, accepted July 7, 2019, date of publication July 11, 2019, date of current version July 29, 2019.

*Digital Object Identifier 10.1109/ACCESS.2019.2928018*

# A Programmable All-Optical Delay Array for Light Detection and Ranging Scene Generation

**YANZE GAO, LANG ZHOU, XIN WANG, HONG YAN, KAIZI HAO, SUHUI YANG, AND ZHUO LI**
School of Optics and Photonics, Beijing Institute of Technology, Beijing 100081, China

Corresponding author: Zhuo Li (lizhuo@bit.edu.cn)

This work was supported by the National Natural Science Foundation of China under Grant 61741502, Grant 61835001, and Grant 61875011.

**ABSTRACT** Light detection and ranging (LiDAR) scene generator is an important device in the LiDAR guidance hardware-in-the-loop (HWIL) simulation system. It generates simulated optical LiDAR scenes under laboratory conditions. A simulated LiDAR scene consists of an array of laser return signals with different intensities and time delays. The intensity of a return signal is determined by the target albedo and the target distance. The time delay of a return signal is determined by the target distance. A time delay array system is crucial for the LiDAR scene generation. In this paper, a programmable all-optical delay array system using an optical true-time-delay (OTTD) method is proposed. It can generate laser return signals with large-signal array size, long delay range, and high delay resolution. The signal array size of the generated LiDAR scene is 32 × 32. The depth of field (DOF) of the LiDAR scene is 19.2 m, which can be placed at different distances from 5.1 to 2481.6 m. The distance resolution is 0.3 m. The all-optical delay array system can also be extended to support tests of the LiDAR guidance systems with larger sensor arrays.

**INDEX TERMS** Laser radar, test equipment, delay systems, optical arrays, optical devices, simulation, optical scene generation, hardware in the loop simulation.

## I. INTRODUCTION

Light detection and ranging (LiDAR) based imaging is an active detection technology with high spatial resolution and strong anti-interference ability. It has many applications in both civilian and military fields, such as 3D mapping, machine vision, obstacle avoidance and precision guidance [1]–[4]. Generally, there are two main types of LiDAR: the frequency-modulated-continuous-wave (FMCW) LiDAR and the time-of-flight (TOF) LiDAR. The LiDAR scene generation concept discussed in this paper applies to the TOF LiDAR, and the term LiDAR mentioned later in this paper refers to the TOF LiDAR. This kind of LiDAR transmits a short laser pulse to illuminate a target and senses the return signals reflected by the target. By measuring the time delays of the return signals relative to the transmitted laser pulse (i.e., the time of flight), the LiDAR system constructs a 3D image of the LiDAR scene.

A LiDAR system transmits a laser pulse to illuminate a target and senses the return signal reflected by the target, as shown in Fig. 1. Suppose $L$ is the target distance, $t$ is the time delay of the return signal relative to the transmitted laser pulse. Easy to know that the laser pulse has traveled twice the target distance during the time delay. So the target distance is calculated by:

$$L = c \cdot t/(2n_{air}) \tag{1}$$

where $c$ is the speed of light in vacuum, $n_{air}$ is the refractive index of the atmosphere. In this paper, a simplified model with $n_{air} = 1$ is considered.

A LiDAR-based imaging system transmits a short laser pulse to illuminate a spatial scene and uses a sensor array to sense the return signals reflected by different parts of the scene, as shown in Fig. 2. By measuring the time delays of

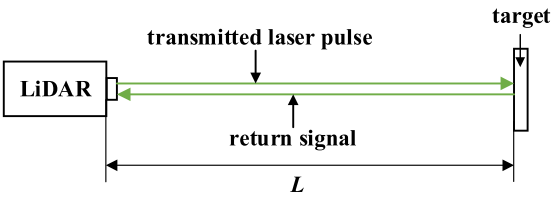


**FIGURE 1.** Schematic diagram of LiDAR.

The associate editor coordinating the review of this manuscript and approving it for publication was Sukhdev Roy.

  

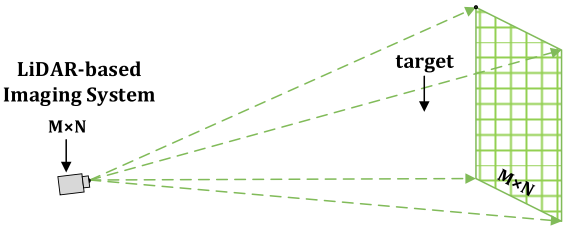


**FIGURE 2.** Schematic diagram of LiDAR-based imaging system.

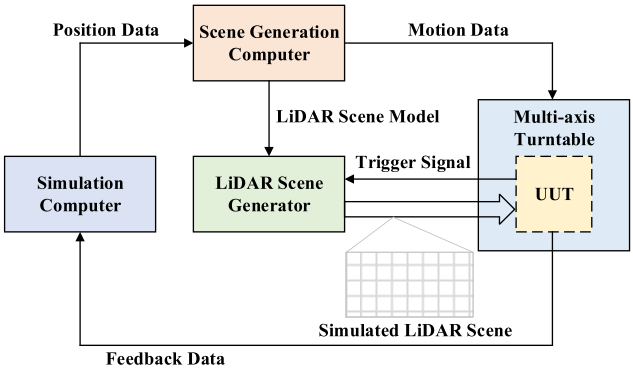


**FIGURE 3.** Block diagram of a LiDAR guidance HWIL simulation system.

the return signals, the system constructs a 3D image of the LiDAR scene.

Hardware-in-the-loop (HWIL) simulation is an effective approach for testing and evaluation in the development of LiDAR guidance system [5]–[10]. It can overcome the disadvantages of outfield test, e.g. high cost, long period, being sensitive to weather conditions, and poor repeatability of data. A typical LiDAR guidance HWIL simulation system usually includes a simulation computer, a scene generation computer, a LiDAR scene generator and a multi-axis (e.g., three-axis or five-axis) turntable, as shown in Fig. 3. A LiDAR guidance system is mounted on the multi-axis turntable as a unit under test (UUT). The simulation computer is the host for the UUT dynamics model and acts as the master control of the HWIL system. The scene generation computer receives position data from the simulation computer and generate a digital LiDAR scene model. The LiDAR scene generator receives the scene model data and generates an optical LiDAR scene (i.e., array laser return signals with different intensities and time delays) when it is triggered by the UUT. The simulated LiDAR scene is then projected into the UUT through an optical projection system. Finally, the UUT returns feedback data to the simulation computer to close the loop [6].

One of the most important functions of LiDAR scene generator is to simulate the time delays of the return signals because the LiDAR system constructs a 3D image by measuring the time delays. The time delay performances of a LiDAR scene generator include:

(1) delay resolution, which has to be better than the time measurement resolution of the LiDAR under test;

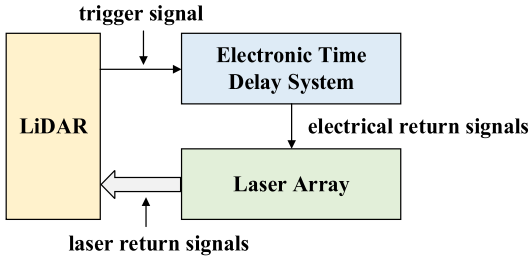


**FIGURE 4.** Schematic diagram of the LiDAR scene generator using electronic time delay system.

(2) delay range, which needs to cover the detection range of the LiDAR under test;

(3) delay array size, which needs to match the sensor array size of the LiDAR under test.

Currently, researchers mainly use electronic time delay system to generate return signals with different time delays [5]–[10], as shown in Fig. 4. The LiDAR system transmits a trigger signal to the electronic time delay system at the same time when it emits a laser pulse. The counter of the electronic time delay system starts counting when it is triggered. Electrical return signals with different amplitudes and time delays are then generated and sent to drive a laser array to transmit laser return signals.

Electronic time delay modules with long time delay range and high time delay resolution are commercially available. However, the cost of the electronic time delay system will become extremely high when the sensor array size of the LiDAR under test becomes large. In a previous paper from our team [7], a LiDAR scene generator with a time delay resolution of 10 ns and 108 time delay channels was developed using electronic time delay modules provided by National Instruments (NI, USA). Its electronic time delay system consists of a controller module (Pxie-8135), a timing and synchronization module (Pxie-6674T), two FPGA modules (Pxie-7972R), two IO adapter modules (Pxie-6581B), and a chassis (Pxie-1082). One FPGA module and one IO adapter module form one time delay module with a time delay resolution of 10 ns and 54 time delay channels. For a LiDAR system with a larger sensor array, such as $32\times32$, the required number of time delay channels reaches 1024. Integrating thousands of electronic time delay channels is a big challenge and extremely expensive at the current state of the art. Moreover, 1024 lasers are needed to generate the laser return signals, which is also very costly.

The purpose of this paper is to explore a feasible solution to integrate large-size time delay arrays for LiDAR scene generation at an acceptable cost. Our approach is to build an all-optical delay system based on the optical true-time-delay (OTTD) method. The principle of OTTD method is to let the laser pulse propagate a distance in free space or in a transmission medium (such as fiber) to get the desired time delay. It has been used in many information processing systems. For example, in optical measurement systems, it is used for

signal synchronization and gating [11]–[13]. In optical communication systems, it is used for buffering optical signals and synchronizing optical data packets [14], [15]. In optically controlled phased array antenna (OCPAA) systems, it is used for constructing the phase shifting network [16]–[19]. The time delay resolution of the OTTD method depends on the length precision of the optical delay path. For example, to achieve a time delay resolution of 2 ns, the required precision of the delay fiber length is 0.4 m (supposing the refractive index of fiber is 1.5). However, the OTTD method does not perform well in achieving long time delay. For example, to achieve a time delay of 10 $\mu$s, 2 km long fiber is needed. This limits the large-array-size integration of OTTD channels. In a LiDAR scene generator, thousands of time delay channels are arranged as a 2D array in space. The range of LiDAR scenes it simulates usually covers a few hundred meters to a few kilometers. Correspondingly, the time delay range of a single OTTD channel needs to reach an order of microseconds to milliseconds. The required fiber length needs to be tens of meters to tens of kilometers. Therefore, simply integrating thousands of OTTD channels into optical delay array is very complicated and not practical for LiDAR scene generation in cost and volume.

A programmable all-optical delay array for LiDAR scene generation is proposed in this paper. It is designed based on two methods called ''delay-based scene slicing'' and ''programmable space routing''. The all-optical delay array system has no photoelectric conversion process and can directly delay the original transmitted laser pulse. The signal array size is 32×32. It can simulate a detailed LiDAR scene with a depth of field (DOF) of 19.2 m. The DOF can be placed at different distances from 5.1 m to 2481.6 m. The distance resolution is 0.3 m. The expected cost is about 1/10 of the cost of the solution using NI electronic time delay modules and 1024 lasers.

The paper is arranged as follows: in Section I, the research background and current problems for LiDAR scene generation are reviewed. In Section II, the methods for implementing the programmable all-optical time delay array are introduced. In Section III, a LiDAR scene generator is designed, and the time delay performance is analyzed. In Section IV, the test results of a programmable fiber delay system are presented. In Section V, some conclusions are made.

## II. METHODOLOGY

### A. LIDAR SCENE MODELING

A LiDAR-based imaging system detects unknown spatial scenes, whereas a LiDAR scene generator generates simulated optical LiDAR scenes based on pre-modeled LiDAR scene models. A LiDAR scene model consists of $M \times N$ points, each of which is denoted as

$$P = (m, n, I, t).$$

Each $\boldsymbol{P}$ point describes the necessary information for a return signal in the LiDAR scene, where ($m$,$n$) represents the spatial position of the return signal, $I$ represents the intensity of the return signal, and $t$ represents the time delay of the return signal. $M \times N$ is the sensor array size of the LiDAR system under test, and $m \in [1, M]$, $n \in [1, N]$. Suppose the detection distance range of the LiDAR system is $[L_{\min}, L_{\max}]$, and the value range of the $t$ component is $[t_{\min}, t_{\max}]$, then according to (1):

$$t_{\min} = 2L_{\min}/c, t_{\max} = 2L_{\max}/c.$$

Fig. 5 is a typical LiDAR scene model indicated by ($m$,$n$,$t$) with the $I$ component omitted.

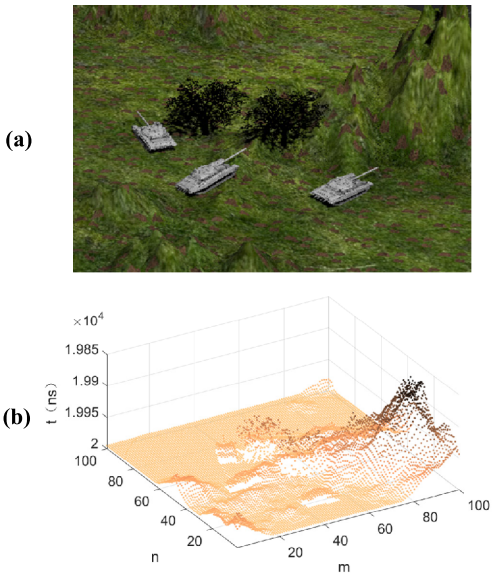


**FIGURE 5.** Illustration diagram of a typical LiDAR scene model (100×100). (a) The computer model of the LiDAR scene. (b) The LiDAR scene model indicated by (*m*,*n*,*t*).

### B. DELAY-BASED SCENE SLICIING

In this Section, the LiDAR scene model is further processed by a method called ''delay-based scene slicing''. This method is similar to the computer tomography (CT) in the medical imaging application. The difference is that the LiDAR scene model is sampled into time delay slices according to different time delay values here, whereas an object is sampled into cross sections at different space positions by the CT machine. Take a pyramid shape LiDAR scene model as an example, as shown in Fig. 6. The LiDAR scene model is sliced along the optical axis of the receiving optics every $\Delta t$ time (Fig. 6(a)). Each time delay slice contains a set of $\boldsymbol{P}$ points.

Suppose $\delta$ is the distance resolution of the LiDAR system. Then the time delay resolution is: $\tau = 2\delta/c$. The LiDAR scene model is sliced into time delay slices with respect to $\tau$(i.e., the two adjacent time delay slices have the time interval of $\Delta t = \tau$). The time delay value of the $i$th time delay slice equals to:

$$t_i = t_{\min} + (i-1) \cdot \Delta t, \quad i = 1, 2, 3, \cdots, A \qquad (2)$$

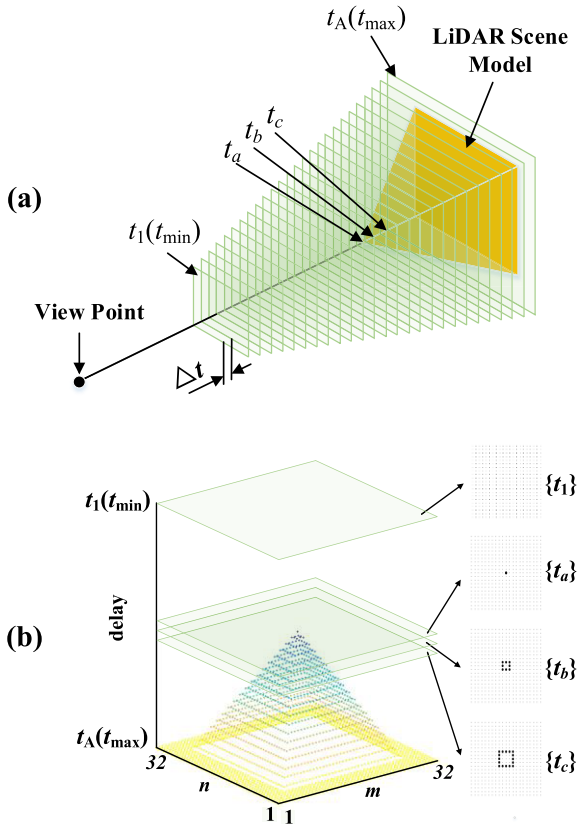


**FIGURE 6.** Schematic diagram of the delay-based scene slicing process for a pyramid shape LiDAR scene model with an array size of 32×32. (a) The delay-based scene slicing process over [$t_{min}$, $t_{max}$]. (b) Four time delay slice examples.

where $\boldsymbol{A}$ is the total number of the time delay slices:

$$A = \lceil (t_{\max} - t_{\min})/\Delta t \rceil + 1 \tag{3}$$

As mentioned in Section II.A, a LiDAR scene model contains $M \times N$ $\boldsymbol{P}$ points, each of which is denoted as $P = (m, n, i, t)$. Each $\boldsymbol{P}$ point describes the necessary information for a return signal in the LiDAR scene. Here we define a time delay slice $\{t_i\}$ as a set of $\boldsymbol{P}$ points whose $t$ components equal to $t_i$. Then from the time delay slice $\{t_i\}$, we can know the intensities and the spatial positions of all the return signals whose time delay values equal to $t_i$.

Suppose all the $M \times N$ points in a LiDAR scene model constitute a superset $P_{all}$. Then any time delay slice is a subset of $P_{all}$:

$$\{t_i\} \subseteq P_{all}, \quad i \in [1, A] \tag{4}$$

The number of points included in one time delay slice varies from 0 to $M \times N$. Any two time delay slices are mutually exclusive:

$$\{t_a\} \cap \{t_b\} = \emptyset, \quad a, b \in [1, A] \tag{5}$$

That is to say, any $\boldsymbol{P}$ point in the LiDAR scene model only belongs to a unique time delay slice, and does not appear on other time delay slices.

Fig. 6(b) is an illustration of four time delay slice examples which are indicated as $\{t_1\}$, $\{t_a\}$, $\{t_b\}$, and $\{t_c\}$. The points included in each time delay slice are marked with black dots. It can be seen that $\{t_1\}$ is an empty slice. $\{t_a\}$, $\{t_b\}$, and $\{t_c\}$ are non-empty slices. And $\{t_1\}$, $\{t_a\}$, $\{t_b\}$, and $\{t_c\}$ are mutually exclusive.

### C. PROGRAMMABLE SPACE ROUTING

All the laser return signals which belong to the time delay slice $\{t_i\}$ should have the same time delay $t_i$. A laser pulse $T_i$ with time delay $t_i$ and pulse width $T$ is used to represent the laser return signal in the time delay slice $\{t_i\}$. $T_i$ is defined as:

$$T_i = \begin{cases} I_{ds}, & t \in [t_i, t_i + T] \\ 0, & t \notin [t_i, t_i + T] \end{cases} \tag{6}$$

where $I_{ds}$ is the intensity of $T_i$:

$$I_{ds} = \beta \cdot I_{\max} \cdot M \times N \tag{7}$$

where $\beta$ is an area scaling factor which will be explained in Section II.D, $I_{max}$ is the maximum $I$ component of all $\boldsymbol{P}$ points in the LiDAR scene model. The timing diagram of $T_i$ is shown in Fig. 7, where $T_0$ is the original transmitted laser pulse with an intensity $I_0$.

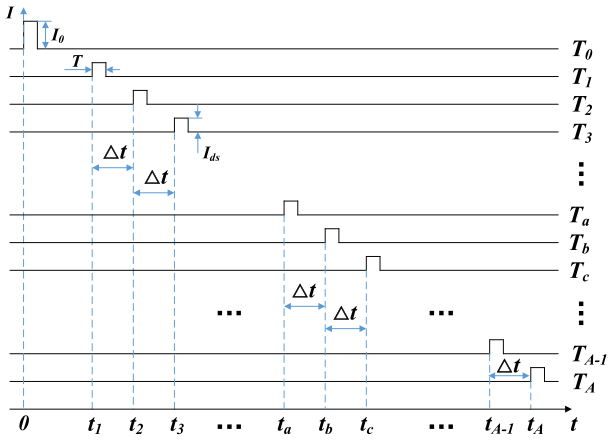


**FIGURE 7.** Timing diagram of the delay-slice signal $T_i$.

$T_i$ is referred to as the delay-slice signal later in this paper. The optical LiDAR scene can be generated by routing $T_i$ to the appropriate spatial positions and modulating its intensity. This process is called the programmable space routing. In this paper, a spatial light modulator (SLM) is used to implement the space routing process. The principle is shown in Fig. 8.

The area of the SLM is divided into $\boldsymbol{A}$ regions named as modulation units. Each modulation unit is illuminated by a delay-slice signal $T_i$. The active area of each modulation unit contains $M \times N$ pixels, this pixel number corresponds to the pixel number of the LiDAR scene we want to generate. For example, assuming that we want to generate a LiDAR scene with 32×32 pixels, then we choose 50×50 as the pixel number of a modulation unit because there should be a

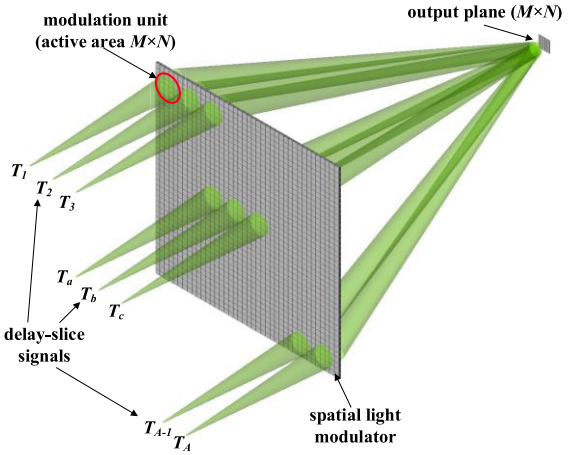


**FIGURE 8.** Schematic diagram of the programmable space routing process.

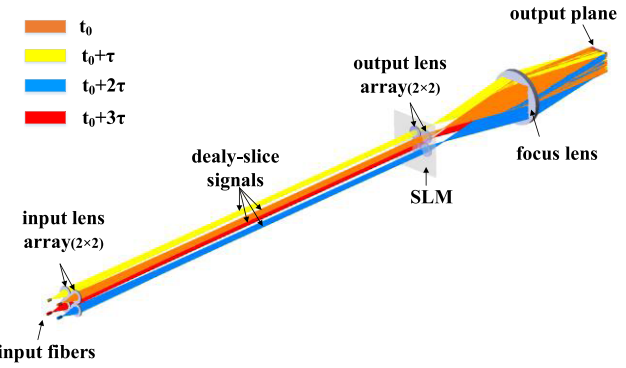


**FIGURE 9.** Schematic diagram of the programmable space routing process between 4 delay-slice signals and 9 laser return channels.

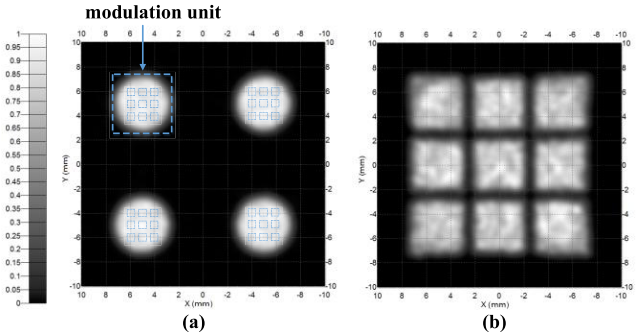


**FIGURE 10.** Illustration diagram of light intensity distribution in the simulated space routing system. (a) The illumination spot on each modulation unit. (b) The output image of each modulation unit on the output plane.

margin between adjacent modulation units. The outputs from each modulation unit are imaged onto the same area on the output plane. Since each delay-slice signal has a different time delay, then each modulation unit will be sequentially illuminated at different times. Therefore, the output image of each modulation unit will appear on the output plane in the time sequence of the time delay slices. The transmittance of individual pixel in each modulation unit determines whether the delay-slice signal illuminated on it can pass through it and eventually reach the output plane. A grayscale image can be used to program the SLM to control the transmittance of each pixel on the SLM, thereby controlling the intensities and time delays of the delay-slice signals arriving at different spatial positions on the output plane.

A simulated LiDAR scene is a spatial 2D array of optical signals with different intensities and time delays. And the function of the space routing process described above is exactly to control the intensities and time delays of the delay-slice signals hitting different spatial positions of the output plane, thus can be used for LiDAR scene generation. The output plane is then projected onto the sensor array of the LiDAR system under test by an optical projection system to complete the LiDAR scene generation.

We simulate the programmable space routing process with a simple model as shown in Fig. 9. This simple model requires routing between 4 delay-slice signals and 3×3 laser return channels. The time delay values of the 4 delay-slice signals are $t_0$, $t_0+\tau$, $t_0+2\tau$, and $t_0+3\tau$. Different colors are used to represent these 4 delay-slice signals. The delay-slice signals enter the space routing system through the input fibers. The core diameter of each input fiber is 200 $\mu$m. The input lens array (2×2) is the same as the output lens array (2×2), and each individual lens has a focal length of 15 mm and a diameter of 10 mm. The focus lens has a focal length of 80 mm and a diameter of 40 mm. The SLM in this simulated model is a hypothetical device with a pixel size of 0.8 mm × 0.8 mm and a pixel pitch of 1 mm (a real SLM will have a much smaller pixel size and pixel pitch). The input lens array images the end faces of the 4 input fibers onto the 4 modulation units on the SLM, so that each modulation unit is uniformly illuminated. The illumination spot on each modulation unit is shown in Fig. 10(a). Each modulation unit has 3×3 active pixels, as shown by the small dashed blue squares in Fig. 10(a). The 4 modulation units are respectively imaged onto the same area on the output plane by the output imaging optics (i.e., the output lens array and the focus lens). The output image of each modulation unit on the output plane has 3×3 pixels corresponding to the 3×3 laser return channels, as shown in Fig. 10(b). The size of each pixel of the output image is approximately 4 mm × 4 mm.

The delay-slice signals arriving at different pixels on the output plane are selected by programming the transmittance of the pixels in the SLM modulation units. As shown in Figure 11.

The 4 modulation units on the SLM are programmed according to the pixel patterns shown in Fig. 11(a). And 9 delay-slice signals with different time delays are finally arrived at the output plane, as shown in Fig. 11(c). Note that the pixel patterns in Fig. 11(a) adopt a binary mode (i.e., white color represents the maximum transmittance of the pixel, and black color represents the minimum transmittance of the pixel). However, for LiDAR scene generation applications,

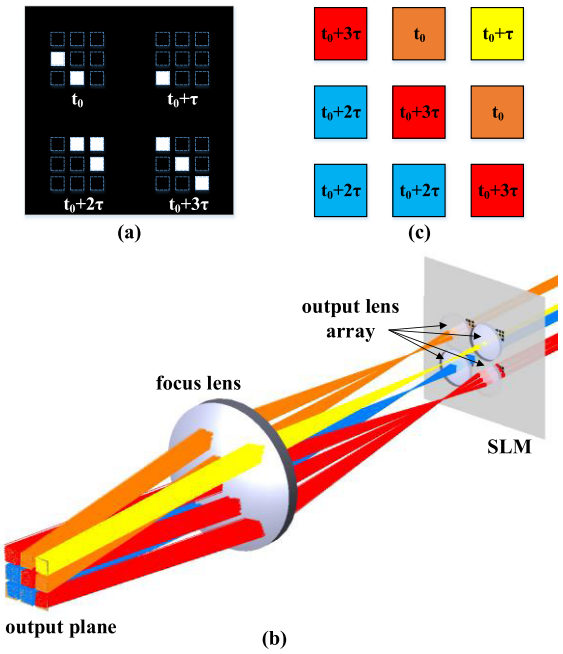


**FIGURE 11.** Schematic diagram of the signal routing process by programming the SLM. (a) The pixel pattern on each modulation unit. (b) Ray tracing. (c) The time delay value of the delay-slice signal arriving at each pixel on the output plane.

the transmittance of the pixels in the $i$th modulation unit needs to be programmed according to the $\boldsymbol{P}$ points included in time delay slice $\{t_i\}$. The pixel position in the active area of the $i$th modulation unit is represented by $(m,n,i)$. Then the gray level of pixel $(m,n,i)$ is given by:

$$g(m,n,i) = \begin{cases} 2^G \cdot I_{m,n}/I_{\max}, & P_{m,n} \in \{t_i\} \\ 0, & P_{m,n} \notin \{t_i\} \end{cases} \tag{8}$$

where $I_{m,n}$ is the $I$ component of the point $P_{m,n} = (m, n, I, t)$, and $G$ is the bit-depth of the SLM (typical values: 8, 10, 12, 16, etc.).

### D. SHARED DELAY AND DOF LIDAR SCENE MODEL

In programmable space routing system, the area of the SLM is divided into $\boldsymbol{A}$ modulation units (Fig. 8). Each modulation unit has an active area with $M \times N$ pixels. Therefore, the number of pixels of the SLM is at least $M \times N \times \boldsymbol{A}$. In addition, the necessary margin between adjacent modulation units is required, which also occupies a portion of the SLM pixels. As shown in Fig. 12, the modulation unit is a squire containing $M' \times N'$ pixels. The active area of a modulation unit is a rectangle containing $M \times N$ pixels. The illumination spot on each modulation unit is a circle. Then:

$$M' = N' > \sqrt{M^2 + N^2} \tag{9}$$

Assuming that the area of the active area is $S_{active}$ and the area of the illumination spot is $S_{spot}$, then the area scaling factor in (7) is:

$$\beta = S_{spot}/S_{active} \tag{10}$$

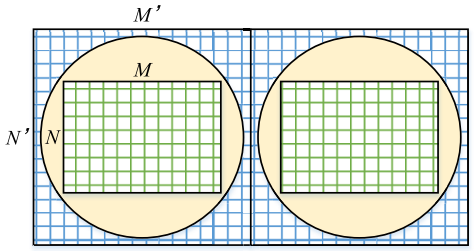


**FIGURE 12.** Illustration diagram of the modulation unit, the illumination spot, and the active area of the modulation unit.

**TABLE 1.** Parameters of a LiDAR system.

| Parameters | Value |
|---|---|
| Wavelength | 1.064 μm |
| Detection range | 150 m - 1500 m |
| Distance resolution | 0.3 m |
| Array size | 32×32 |
| Repeat frequency | 20 Hz |

The SLM needs to have at least $M' \times N' \times \boldsymbol{A}$ pixels to support the routing between $\boldsymbol{A}$ delay-slice signals and $M \times N$ laser return channels. This means a SLM can only support the routing for a limited number of delay-slice signals. However, the number of time delay slices will be very large if the LiDAR scene model is sliced over the entire time delay range from $t_{\min}$ to $t_{\max}$(Fig. 6(a)). Take a LiDAR system shown in Table 1 as an example.

According to Table 1:

$$L_{\min} = 150 \text{ m}, L_{\max} = 1500 \text{ m}, \delta = 0.3 \text{ m}, M = N = 32.$$

Then we have:

$$t_{\min} = 1\ \mu\text{s}, t_{\max} = 10\ \mu\text{s}, \tau = \Delta t = 2 \text{ ns}, \boldsymbol{A} = 4501.$$
$$M' = N' > 32\sqrt{2}$$

Here $M'$ and $N'$ take the minimum value of 46. In order to support the routing between 4501 delayed slice signals and 1024 laser return channels, the number of pixels required for the SLM is at least:

$$M' \times N' \times \boldsymbol{A} = 9524116 \approx 3087 \times 3087.$$

The SLM with such large pixel array size is expensive. Fortunately, we found that some features of the LiDAR scene model can help us simplify the time delay system. Generally, the targets detected and tracked by a LiDAR guidance system are in the space where the laser is not obscured, that is, there is no obstruction between the target and the LiDAR view point. The LiDAR scene generator only needs to accurately simulate the return signals in a certain spatial range before and after the target to provide enough scene details for the HWIL simulation test.

As shown in Fig. 13. The $t$ component of all the $\boldsymbol{P}$ points in the LiDAR scene model is greater than a certain time delay

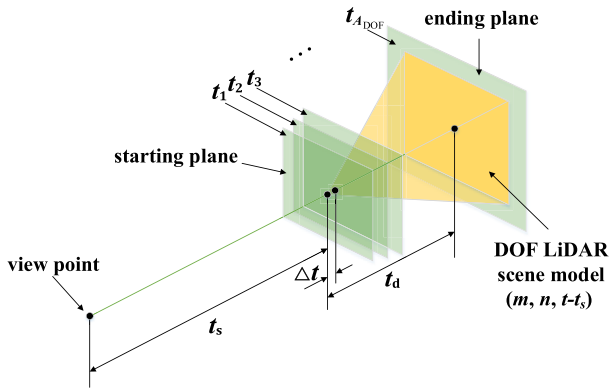


**FIGURE 13.** Illustration diagram of the DOF of the LiDAR scene.

value, which is the time delay of the return signal corresponding to the point closest to the view point. This minimum time delay is called the shared delay which is denoted as $t_s$. The distance of this closest point is denoted as $L_s$, then:

$$t_s = 2L_s/c, t_s \in [t_{\min}, t_{\max}] = [1\mu s, 10\mu s].$$

There is a starting plane in front of the target and an ending plane behind the target in the direction of the optical axis of the receiving optics. The space between the starting plane and the ending plane is the scene whose return signals need to be accurately simulated. In this paper, the distance range between the starting plane and the ending plane is called the depth of field (DOF) of the LiDAR scene and is denoted as $L_d$. The length of $L_d$ is determined by the size of the target that the LiDAR system needs to detect. In this paper, $L_d$ is taken as 19.2 m. Then the time delay range of the DOF of the LiDAR scene is:

$$t_d = 2L_d/c = 128 \text{ ns}.$$

A new scene model is obtained by subtracting the shared delay $t_s$ from the $t$ component of all $\boldsymbol{P}$ points in the original LiDAR scene model:

$$(m, n, I, t) \rightarrow (m, n, I, t - t_s).$$

Then check the time delay values of all points in this new model and discard the points with time delay values greater than $t_d$:

$$(m, n, I, t - t_s \leq t_d)\checkmark, \quad (m, n, I, t - t_s > t_d) \times .$$

This new scene model contains the time delay information of the laser return signals reflected by the objects in the original LiDAR scene from the distance $L_s$ to the distance $(L_s + L_d)$. It contains detailed information about the LiDAR scene that can meet most of the requirements of the HWIL simulation test. The distance range this new scene model represents is the DOF of the original LiDAR scene. Therefore, this new scene model is called the DOF LiDAR scene model.

Note that the shared delay $t_s$ ranges from 1 $\mu$s to 10 $\mu$s, whereas the delay range $t_d$ of the DOF is only 128 ns. This feature of LiDAR scene model helps to simplify the time delay system. A multiplexed time delay channel can be shared by all the laser return signals to get the shared time delay with a long time delay range, and a programmable space routing system is used to generate the DOF of LiDAR scene with a short time delay range but sufficient details. The DOF LiDAR scene model is sliced using the delay-based scene slicing method introduced in Section II.B. The total number of time delay slices of the DOF LiDAR scene model is:

$$A_{DOF} = t_d/\tau = 64.$$

This makes it possible to find a suitable SLM to perform the programmable space routing process.

## III. HARDWARE IMPLEMENTATION

In this section, the hardware system of the programmable all-optical delay array is designed. The hardware system includes a multiplexed delay channel, a delay-slice signal generator and a space routing system, as shown in Fig. 14.

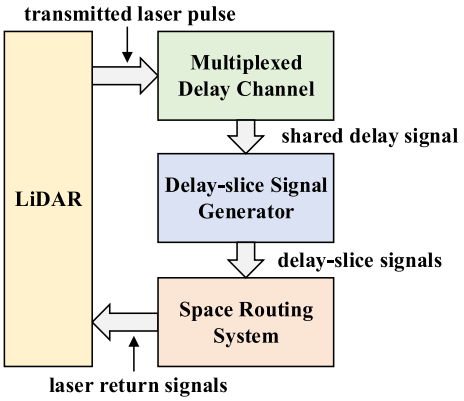


**FIGURE 14.** Block diagram of the programmable all-optical delay array system.

### A. MULTIPLEXED DELAY CHANNEL

The time delay values of all return signals in the LiDAR scene are greater than $t_s$, which means they all share the same $t$ component of $t = t_s$. A multiplexed delay channel is used first to make the transmitted laser pulse obtain a shared delay of $t_s$. The structure of the multiplexed delay channel is shown in Fig. 15.

The multiplexed delay channel consists of an attenuator, two 1×2 optical switches, twelve 2×2 optical switches and thirteen delay fibers (multimode fiber, 200/220 $\mu$m).

The transmittance of the attenuator is:

$$\alpha = I_{ds} \cdot A_{DOF}/(I_0 \cdot \gamma). \tag{11}$$

where $I_{ds}$ is the intensity of the delay-slice signal given by (7), $A_{DOF} = 64$ is the number of time delay slices of the DOF LiDAR scene model, $I_0$ is the intensity of the original transmitted laser pulse, $\gamma$ is the transmittance of the multiplexed delay channel.

The theoretical time delay of the $k$th delay fiber is:

$$\Delta\tau_k = \tau \cdot 2^{k-1}, \quad k = 1, 2, 3, \cdots, 13 \tag{12}$$

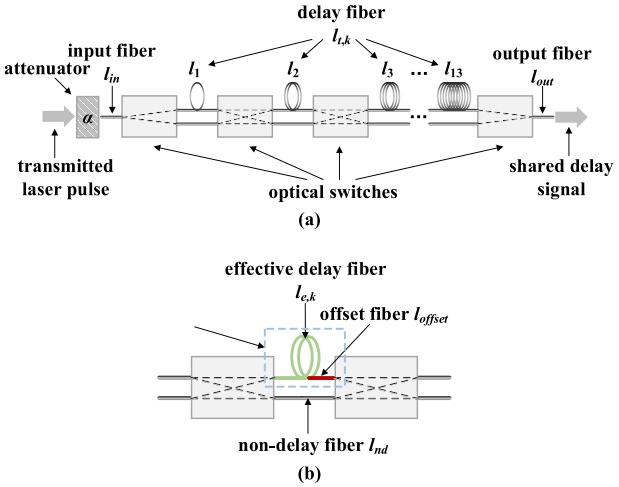


**FIGURE 15.** Structure of the multiplexed delay channel. (a) Internal optical path. (b) Fibers between two adjacent optical switches. ($l_{in}$ is input fiber length, $l_{out}$ is output fiber length, $l_{t,k}$ is the true length of the kth delay fiber,$l_{e,k}$ is the effective delay length of the kth delay fiber, $l_{offset}$ is the length of the offset fiber offsetting the delay caused by the non-delay fiber, $l_{nd}$ is the length of the non-delay fiber connecting the non-delay path of two adjacent optical switches.).

where $\tau$ is the time delay resolution:

$$\tau = l_\tau \cdot n_{fiber}/c \tag{13}$$

where $l_\tau$ is the fiber length resolution of the multiplexed delay channel, $n_{fiber}$ is the refractive index of the delay fiber. The fiber used here has a refractive index of $n_{fiber} = 1.4573$ at 1.064 $\mu$m at room temperature of 25 °C. $\tau = 2$ns, then we have:

$$l_\tau = c \cdot \tau / n_{fiber} = 0.41 \text{ m}.$$

In the multiplexed delay channel, the optical switches are programmable. The internal light path of an optical switch can be programmed by writing "0" or "1" to the optical switch, as shown in Fig. 16. By programming the internal light paths of the optical switches, the laser pulse is guided to pass through different delay fibers to get different time delays.

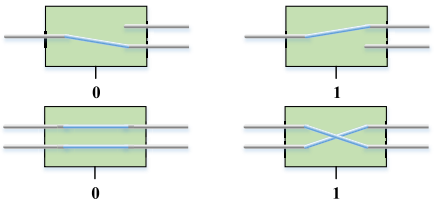


**FIGURE 16.** Schematic diagram of the programming operation of the optical switch.

The maximum time delay of the multiplexed delay channel should be greater than the maximum time delay required by the LiDAR scene generator:

$$t_{s\max} = \sum_{k=1}^{k=13} \Delta\tau_k > \frac{2L_{\max}}{c} \tag{14}$$

The time delay of the effective delay length of the $k$th delay fiber $l_{e,k}$ is $\Delta\tau_k$, then:

$$l_{e,k} = c \cdot \Delta\tau_k / n_{fiber}, \quad k = 1, 2, 3, \cdots, 13 \tag{15}$$

The true length of the $k$th delay fiber $l_{t,k}$ consists of an offset fiber length $l_{offset}$ in addition to the effective delay fiber length $l_{e,k}$:

$$l_{t,k} = l_{e,k} + l_{offset}.$$

The effect of the offset fiber is to offset the time delay caused by the non-delay fiber, and to ensure that the time delay of the delay fiber is $\Delta\tau_k$ longer than the time delay caused by the non-delay fiber. Therefore, the length of the offset fiber equals to the non-delay fiber: $l_{offset} = l_{nd}$. $l_{offset}$ is designed as:

$$l_{offset} = l_\tau = 0.41 \text{ m}.$$

The fiber lengths in the multiplexed delay channel are listed in Table 2.

**TABLE 2.** Fiber lengths in the multiplexed delay channel.

| $k$ | Effective delay length $l_{e,k}$ | True length $l_{t,k}$ |
|---|---|---|
| 1 | 0.41 m | 0.82 m |
| 2 | 0.82 m | 1.23 m |
| 3 | 1.65 m | 2.06 m |
| 4 | 3.29 m | 3.70 m |
| 5 | 6.59 m | 7.00 m |
| 6 | 13.18 m | 13.59 m |
| 7 | 26.35 m | 26.76 m |
| 8 | 52.70 m | 53.11 m |
| 9 | 105.40 m | 105.81 m |
| 10 | 210.80 m | 211.21 m |
| 11 | 421.60 m | 420.01 m |
| 12 | 843.20 m | 843.61 m |
| 13 | 1686.41 m | 1686.82 m |
| Input fiber length | | 0.41 m |
| Output fiber length | | 0.41 m |
| Total length | 3372.40 m | 3378.55 m |

As can be seen from Table 2, the true fiber length of the system is longer than the effective delay fiber length, which causes an insertion time delay. Its value is:

$$t_{ins1} = (3378.55 - 3372.40) \times n_{fiber}/c = 30 \text{ ns}.$$

### B. DELAY-SLICE SIGNAL GENERATOR

The transmitted laser pulse obtains a shared time delay of $t_s$ after passing through the multiplexed delay channel and then enters the delay-slice signal generator. It is then divided into $A_{DOF} = 64$ sub-pulses. The time delay of two adjacent sub-pulses is incremented by $\Delta t = \tau = 2$ ns. Then 64 delay-slice signals are generated.

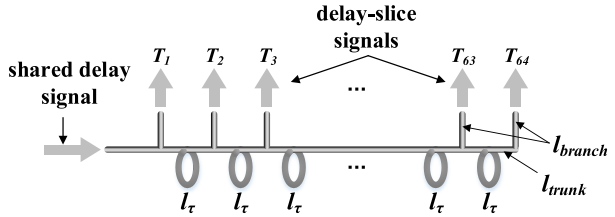


**FIGURE 17.** Structure of the delay-slice signal generator.

The delay-slice signal generator is a fiber (multimode fiber, 200/220 $\mu$m) with branches. The structure is shown in Fig. 17. There is a branch fiber every 0.41 m (i.e.,$l_\tau$ ) along the trunk fiber. The length of the trunk fiber is:

$$l_{trunk} = A_{DOF} \cdot l_\tau = 26.24 \text{ m}.$$

The delay-slice signal generator also has an insertion time delay which is caused by the branch fiber $l_{branch}$. Let

$$l_{branch} = l_\tau = 0.41 \text{ m}.$$

Then the insertion time delay caused by the delay-slice signal generator is:

$$t_{ins2} = l_{branch} \cdot n_{fiber}/c = 2 \text{ ns}.$$

### C. SPACE ROUTING SYSTEM

The signal array size of the LiDAR scene we want to generate is $M \times N = 32 \times 32$. According to (9), $M' = N' > 32\sqrt{2}$. Here $M'$ and $N'$ are taken as 50. The number of delay-slice signals is $A_{DOF} = 64$. Then the number of pixels required for SLM is:

$$M' \times N' \times A_{DOF} = 160000 = 400 \times 400.$$

The parameters of a liquid crystal SLM are shown in Table 3.

**TABLE 3.** Parameters of a liquid crystal SLM.

| Parameters | Value |
|---|---|
| Modulation type | Amplitude modulation |
| Liquid crystal type | Transmissive |
| Pixel array size | 1024×768 |
| Pixel size | 36 μm |
| Bit depth | 8 bits |
| Frame rate | 60 Hz |

The pixel array size of the SLM is 1024×768 which is more than 400×400, thus can be used to perform the space routing process. Fig. 18 shows the structure of the space routing system for 64 delay-slice signals and 1024 laser return channels. 64 delay-slice fibers (i.e., the branch fibers of the delay-slice signal generator) are arranged in an 8×8 array. Their end faces are imaged on the corresponding modulation units on the SLM by the input lens array (8×8). The central area of the SLM with a pixel array size of 400×400 is

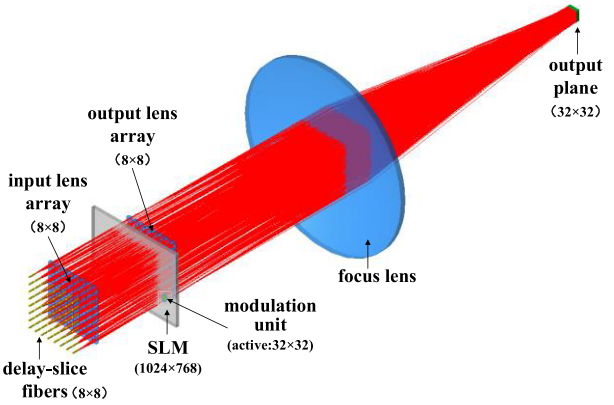


**FIGURE 18.** Structure of the space routing system for 64 delay-slice signals and 1024 laser return channels.

divided into 8×8 modulation units. Each modulation unit has 50×50 pixels with an active area of 32×32 pixels. The outputs of all modulation units are imaged on the output plane by the imaging optics consisting of an output lens array (8×8) and a focus lens. The output image on the output plane consists of 32×32 pixels corresponding to the 1024 laser return channels.

Since the main purpose of this paper is to explain the concept of the programmable space routing, the optical systems are not designed in detail here, only the effect they should achieve are given.

In the space routing system, the delay-slice signal travels from the end face of the delay-slice fiber to the output plane. The length of this trip will cause insertion time delay. Here this trip length is design as $l_{sr} = 0.6$m, then the insertion delay is:

$$t_{ins3} = l_{sr}/c = 2 \text{ ns}.$$

It should be noted that in the space routing system, the delay-slice signals travel through optical paths of different lengths to the output plane. This means that the space routing system introduces different insertion time delays for different delay-slice signals. Therefore, the actual time delay of each delay-slice signals slightly deviates from their ideal time delay, which causes the scene simulated by the LiDAR scene generator to be distorted.

As shown Fig. 19, the center area of the SLM contains 400×400 pixels. The side length of the central area is: $l_{side} = 400 \times 36$ $\mu$m $= 14.4$ mm. The shortest optical path length of the space routing system (i.e., the central optical path) is designed as: $l_{near} = l_{sr} = 60$ mm. According to the geometric relationship in Fig. 19, the longest optical path length is $l_{far} = 60.86$ mm.

Therefore, the maximum insertion time delay difference caused by the space routing system is:

$$\Delta t_{\text{ins3}} = (l_{far} - l_{near})/c \approx 0.003 \text{ ns}.$$

The maximum scene distortion across the whole DOF is:

$$\Delta L_{DOF} = c \cdot \Delta t_{ins3}/2 \approx 0.45 \text{ mm}.$$

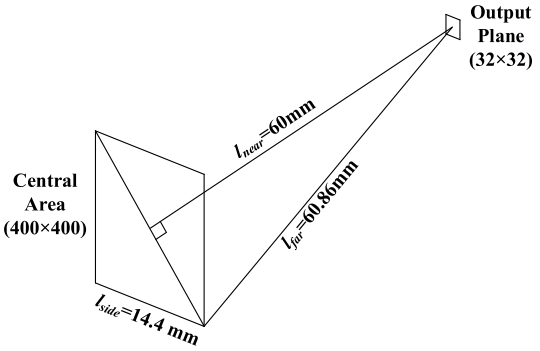


**FIGURE 19.** Illustration diagram of the optical path lengths in the space routing system.

The scene distortion is negligible since it is just 0.45mm, which is 0.15% of the distance resolution (i.e., 0.3 m). However, as the DOF becomes deeper, the central area will increase accordingly. Assuming that $l_{near}$ does not change, then $l_{far}$ has to become longer, which will make the distortion more serious. Therefore, the space routing system must be carefully designed to ensure that the scene distortion is within an acceptable range.

### D. PERFORMANCE ANALYSIS

#### 1) TEMPERATURE IMPACT

The time delay $t$ produced by the fiber length $L$ is:

$$t = L \cdot n/c$$

Both the fiber length $L$ and the fiber refractive index $n$ change with temperature. The time delay change with temperature $\rho$ is:

$$\frac{\partial t}{\partial \rho} = \frac{1}{c}\left[\frac{\partial n}{\partial \rho}L + n\frac{\partial L}{\partial \rho}\right] \tag{16}$$

According to the experimental results of Cohen and Fleming [20], the fiber length change with temperature can be expressed as $\partial L/\partial p = \eta L$, where $\eta \approx 8 \times 10^{-7}/°\text{C}$. The refractive index change with temperature of fused silica fiber is $\partial n/\partial \rho = 1\times10^{-5}/°\text{C}$. The longest delay fiber in the system is $L = 1686.82$ m (Table 2). The fiber refractive index is $n = 1.4573$ at $1.064\mu$m at room temperature of 25 °C. Then:

$$\partial t/\partial \rho \approx 0.06\ ns/°\text{C}.$$

The time delay resolution is 2 ns, with $\pm1$ ns as the accuracy requirement, then the temperature change cannot exceed $\pm16$°C. Therefore, the temperature range of the time delay system is $25\pm16$°C.

#### 2) FRAME RATE

The frame rate of the all-optical delay array system is limited by the SLM and optical switches. The optical switch has a response time of less than 5ms and the maximum switching frequency supported is approximately 200 Hz. The frame rate of the SLM is 60 Hz. Therefore, the maximum frame rate that the entire time delay system can support is 60 Hz.

#### 3) PARAMETER SUMMARY

The analysis of the time delay parameter is simple and will not be described in detail here. The parameters are listed in Table. 4.

**TABLE 4.** Performance of the programmable all-optical delay array.

| Parameters | Value |
|---|---|
| Time delay range | 34 ns – 16544 ns |
| Time delay resolution | 2 ns |
| Number of delay channels | 1024 |
| Distance range | 5.1 m – 2481.6 m |
| Depth of field | 19.2 m |
| Distance resolution | 0.3 m |
| Frame rate | <60 Hz |
| Temperature | $25\pm16$℃ |

## IV. EXPERIMENT

A programmable fiber delay system was developed and tested. It should be noted that the time delay system introduced and tested in this section is only a demo system, which is used to verify the feasibility of the multiplexed delay channel, and is not in accordance with the design parameters in Section III.D. Limited by the processing capabilities of the lab, the demo delay system has a delay resolution of 2 ns and contains only 5 delay fibers. The block diagram of the experiment setup is shown in Fig. 20.

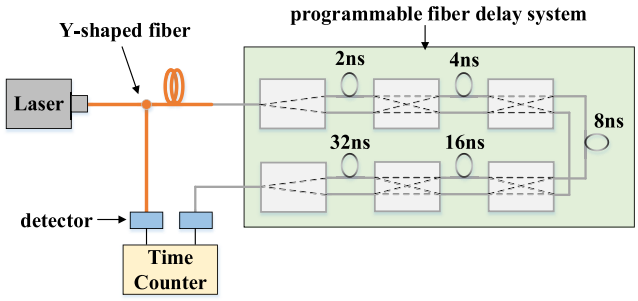


**FIGURE 20.** Block diagram of the experiment setup.

The wavelength of the laser is 1.064 $\mu$m, the pulse width of the laser is 8 ns. The two pigtails of the Y-shaped fiber have the same length. Different time delays are set by programming the six optical switches. The original laser pulse and the delayed laser pulse are converted into electrical signals by two detectors and then sent to the time counter (FCA3100, Tektronix, Inc., USA). The time delay between the two pulses is measured and the results are shown in Fig. 21.

Fig. 21 shows a total of 32 test points from 0 ns to 62 ns, stepping 2 ns. The red circle represents the measured delay and the blue circle represents the set delay. The measured delay minus the set delay results in a minimum value of -0.23 ns and a maximum value of 0.21 ns, thus the integral

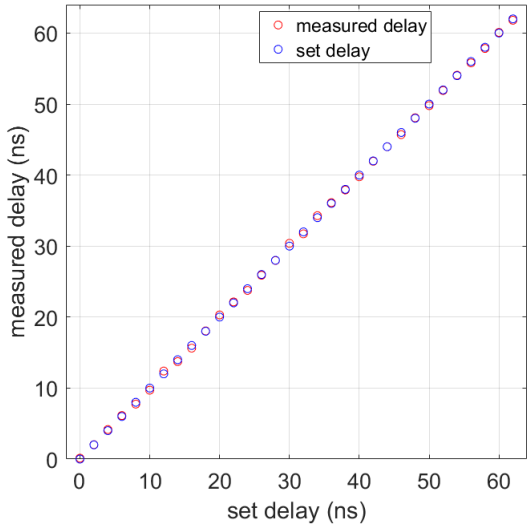


**FIGURE 21.** Test results of the programmable fiber delay system.

non linearity (INL) is −0.115−0.105LSB. The minimum difference between the adjacent two measured delays is 1.67 ns, and the maximum difference is 2.23 ns, so the differential non linearity (DNL) is −0.165 − 0.115LSB.

In this paper, only the design of the multiplexed delay channel is experimentally verified. The hardware of the delay-slice signal generator and the space routing system are under development. The corresponding performance test results will be reported in future papers.

## V. CONCLUSION

In this paper, a programmable all-optical delay array for LiDAR scene generation is proposed, which provides an economical solution for solving the integration problem of thousands of laser return channels. Unlike the traditional design idea of combining single time delay channels into a time delay channel array, we decomposed the LiDAR scene model into two parts, the first part is the shared delay, which has a long time delay range and is shared by all laser return channels. The second part is the DOF LiDAR scene model, which has a short time delay range but contains detailed information of the LiDAR scene. The multiplexed delay channel is applied to achieve the shared delay. The programmable space routing system is applied to achieve the simulation of the DOF LiDAR scene model. The LiDAR scene generator based on this design can be controlled by grayscale image programming.

The programmable all-optical delay array designed in this paper can simulate a detailed LiDAR scene with a signal array size of 32×32 and a DOF of 19.2 m. The DOF can be placed at different distances from 5.1 m to 2481.6 m. The distance resolution is 0.3 m. The number of delay channels can be extended when using multiple SLMs (or using a larger-size SLM) to form the programmable space routing system. The hardware system of LiDAR scene generator based on the design is under development, and the results will be reported in future papers.

## REFERENCES

[1] V. Molebny, P. F. McManamon, O. Steinvall, T. Kobayashi, and W. Chen, "Laser radar: Historical prospective—From the East to the West," *Opt. Eng.*, vol. 56, no. 3, Dec. 2016, Art. no. 031220.

[2] M. A. Powers, "Progress in supercontinuum-based LADAR and its applications to robotic systems," in *Imag. Appl. Opt., OSA Tech. Dig.*, 2013, pp. 1–3, Paper ATh2A.3.

[3] X. Li and Y. Liang, "Remote measurement of surface roughness, surface reflectance, and body reflectance with LiDAR," *Appl. Opt.*, vol. 54, no. 30, pp. 8904–8912, Oct. 2015.

[4] P. Vrancken, M. Wirth, G. Ehret, H. Barny, P. Rondeau, and H. Veerman, "Airborne forward-pointing UV Rayleigh lidar for remote clear air turbulence detection: System design and performance," *Appl. Opt.*, vol. 55, no. 32, pp. 9314–9328, 2016.

[5] H. J. Kim, C. B. Naumann, and M. C. Cornell, "Hardware-in-the-loop projector system for light detection and ranging sensor testing," *Opt. Eng.*, vol. 51, no. 8, Sep. 2012, Art. no. 083609.

[6] J. S. Coker, C. F. Coker, and T. P. Bergin, "Ladar scene generation techniques for hardware-in-the-loop testing," *Proc. SPIE*, vol. 3697, pp. 140–149, Jul. 1999.

[7] R. Xu, X. Wang, Y. Tian, and Z. Li, "Ladar scene projector for a hardware-in-the-loop simulation system," *Appl. Opt.*, vol. 55, no. 21, pp. 5745–5755, 2016.

[8] Y. Gao, X. Wang, Y. Li, L. Zhou, Q. Shi, and Z. Li, "Modeling method of a ladar scene projector based on physically based rendering technology," *Appl. Opt.*, vol. 57, no. 28, pp. 8303–8313, 2018.

[9] J. L. Smith, "Concepts using optical MEMS array for ladar scene projection," *Proc. SPIE*, vol. 5092, pp. 276–287, Sep. 2003.

[10] M. C. Cornell, C. B. Naumann, R. G. Stockbridge, and D. R. Snyder, "LADAR scene projector for hardware-in-the-loop testing," *Proc. SPIE*, vol. 4717, pp. 77–85, Jul. 2002.

[11] L. Richter, H. Mandelberg, M. Kruger, and P. McGrath, "Linewidth determination from self-heterodyne measurements with subcoherence delay times," *IEEE J. Quantum Electron.*, vol. QE-22, no. 11, pp. 2070–2074, Nov. 1986.

[12] A. E. Willner, B. Zhang, L. Zhang, L. Yan, and I. Fazal, "Optical signal processing using tunable delay elements based on slow light," *IEEE J. Sel. Topics Quantum Electron.*, vol. 14, no. 3, pp. 691–705, May/Jun. 2008.

[13] K. Takiguchi, M. Itoh, and T. Shibata, "Optical-signal-processing device based on waveguide-type variable delay lines and optical gates," *J. Lightw. Technol.*, vol. 24, no. 7, pp. 2593–2601, Jul. 2006.

[14] S. Y. Liew, G. Hu, and H. J. Chao, "Scheduling algorithms for shared fiber-delay-line optical packet Switches-part I: The single-stage case," *J. Lightw. Technol.*, vol. 23, no. 4, pp. 1586–1600, Apr. 2005.

[15] S. Jiang, G. Hu, S. Y. Liew, and H. J. Chao, "Scheduling algorithms for shared fiber-delay-line optical packet Switches-part II: The three-stage clos-network case," *J. Lightw. Technol.*, vol. 23, no. 4, pp. 1601–1609, Apr. 2005.

[16] Y. Chen and Y. Chen, "A fully packaged true time delay module for a K-band phased array antenna system demonstration," *IEEE Photon. Technol. Lett.*, vol. 14, no. 8, pp. 1175–1177, Aug. 2002.

[17] T. Tatoli, D. Conteduca, F. Dell'Olio, C. Ciminelli, and M. N. Armenise, "Graphene-based fine-tunable optical delay line for optical beamforming in phased-array antennas," *Appl. Opt.*, vol. 55, no. 16, pp. 4342–4349, 2016.

[18] V. C. Duarte, M. V. Drummond, and R. N. Nogueira, "Photonic true-time-delay beamformer for a phased array antenna receiver based on self-heterodyne detection," *J. Lightw. Technol.*, vol. 34, no. 23, pp. 5566–5575, Dec. 1, 2016.

[19] A. Ben-Amram, Y. Stern, Y. London, Y. Antman, and A. Zadok, "Stable closed-loop fiber-optic delay of arbitrary radio-frequency waveforms," *Opt. Express*, vol. 23, no. 22, pp. 28244–28257, 2015.

[20] L. G. Cohen and J. W. Fleming, "Effect of temperature on transmission in lightguides," *Bell Syst. Tech. J.*, vol. 58, no. 4, pp. 945–951, 1979.

**YANZE GAO** received the B.E. degree from the School of Optics and Photonics, Beijing Institute of Technology, Beijing, China, in 2014, where he is currently pursuing the Ph.D. degree with the Target Simulation Laboratory. His research interests include optical scene generation and hardware-in-the-loop (HWIL) simulation.

**LANG ZHOU** received the B.E. degree from the School of Optics and Photonics, Beijing Institute of Technology, Beijing, China, in 2014, where he is currently pursuing the Ph.D. degree with the Target Simulation Laboratory. His research interests include infrared scene simulation and MEMS technology.

**XIN WANG** was born in Beijing, China, in 1980. She received the Ph.D. degree in physics from the Berlin Institute of Technology, Berlin, Germany, in 2009.

She was a Postdoctoral Researcher with the Institute für Optik und Atomare Physik, Technische Universität Berlin, from 2009 to 2011. Since 2011, she has been an Assistant Professor with the School of Optics and Photonics, Beijing Institute of Technology, Beijing. She has published more than 40 papers in scientific journals. Her current research interests include solid-state lasers, nonlinear optics, infrared optics, and LiDAR.

**HONG YAN** received the B.E. degree from the School of Optics and Photonics, Beijing Institute of Technology, Beijing, China, in 2017, where she is currently pursuing the master's degree with the Target Simulation Laboratory. Her research interests include optical scene generation and hardware-in the-loop (HWIL) simulation.

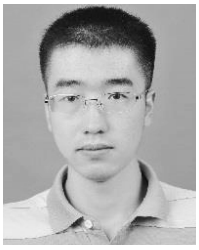

**KAIZI HAO** received the B.E. degree from the College of Electronic Information and Automation, Tianjin University of Science and Technology, in 2015. He is currently pursuing the Ph.D. degree in electronic science and technology with the Beijing Institute of Technology. His research interests include RF/IR beam combiner and hardware-in-the-loop simulation systems.

**SUHUI YANG** was born in Liaoning, China, in 1968. She received the B.S. and M.S. degrees in applied physics from the Changchun University of Science and Technology, Changchun, China, in 1991 and 1994, respectively, and the Ph.D. degree in optics from Jilin University, in 1998.

From 2001 to 2012, she was an Associate Professor with the Beijing Institute of Technology, where she has been a Full Professor, since 2012. She has published more 50 papers in international and domestic journals. Her research interests include solid-state lasers, LiDAR, and underwater detection and ranging.

Dr. Yang is a member of the Chinese Optical Society and the Optical Society of America.

**ZHUO LI** was born in Changchun, Jilin, China, in 1958. He received the Ph.D. degree in optical engineering from the Beijing Institute of Technology, Beijing, China, in 1999.

Since 2002, he has been a Full Professor with the School of Optics and Photonics, Beijing Institute of Technology. His research interests include MEMS optics, infrared technology and applications, and advanced optical instrument. His current research projects focus on optical target simulation technology in the hardware-in-the-loop simulation field, such as infrared dynamic scene generation technology, RF/infrared composite simulation technology, and LiDAR scene generation technology. He is a member of the Chinese Optical Society, the China Ordnance Society, and the Chinese Society of Astronautics.